# Particle Size Effects on the Order-Disorder Phase Transition in [(CH)<sub>3</sub>NH<sub>2</sub>]Mg(HCOO)<sub>3</sub>

Steven A. LoCicero,† Carolyn M. Averback,† Ulyana Shumnyk,† Eun Sang Choi,§ Daniel R. Talham\*,†

†Department of Chemistry, University of Florida, Gainesville, FL 32611-7200, United States §National High Magnetic Field Lab, Tallahassee, FL 32310 United States KEYWORDS: Metal-organic frameworks, Formate perovskites, Mesoscale.

ABSTRACT: Mesoscale particles ranging from 2.3 µm down to 180 nm of dimethylammonium magnesium formate, DMMgF, are generated, and characteristics of the known solid-solid phase transition, in which dimethylammonium ions residing in cavities of the metal formate framework undergo an order-disorder transition, are investigated. Detected by powder X-ray diffraction, the mesoscale particles undergo the same solid-solid phase change characterized for bulk samples, but calorimetry measurements reveal the phase transition temperature decreases in the reduced size particles from 263 K for the bulk materials to 251 K for the 180 nm particles, while the thermal hysteresis associated with the transition increases as the particles become smaller. Despite the solid-solid phase change, the mesoscale particles are too small to detect the pyroelectric current observed for the bulk. Taken together, the changes with particle size point to the elastic framework distortion as the determinant of the phase transition temperature in DMMgF. Synthetic challenges associated with the isolation of reduced size particles, specifically the role of the kinetic product magnesium formate dihydrate, are described.

#### **INTRODUCTION**

Dimethylammonium metal formates (DMMF. [(CH<sub>3</sub>)<sub>2</sub>NH<sub>2</sub>]M(HCOO)<sub>3</sub>) were first reported in 1973,<sup>1</sup> although interest in the DMMF family greatly accelerated when examples of the lead-free ABX<sub>3</sub> type perovskites were reported to be ferroelectric<sup>2</sup> and multiferroic.<sup>3</sup> While subsequent work has shown that examples of proper ferroelectric behavior is limited within this family,4-6 with other members more likely characterized as improper ferroelectrics,5,7 interest remains in the broader family of formate perovskites because they are easily prepared8-11 and offer a rich range of dielectric response, applications<sup>12-14</sup> of which often rely on high surface area material morphologies with small length scales. 15-17 The present study was undertaken to better understand how changes in the surface to volume ratio in DMMF particles change the dielectric response and associated structural changes, and to learn about the driving forces behind the phase transition.

DMMF's consist of octahedrally coordinated divalent metal ions bridged by formate, creating a ReO<sub>3</sub>-type framework wherein dimethylammonium ions reside to maintain charge balance. <sup>18</sup> The dimethylammonium ion is disordered across three positions in which the cation hydrogen bonds with the formate oxygen atom. <sup>19</sup> The cation motion decreases when cooled leading to a disorder-order transition, characterized by cooperative hydrogen bonding with alteration of the metal-formate framework and spontaneous polarization across the material. <sup>2,8,19,20</sup> Synthetic modularity has been used to gain insight into the parameters affecting the driving forces of the phase transition. Varying the metal

ion has led to differences in order-disorder transition temperature from 160 - 270 K,<sup>2,3,8</sup> although disentangling the individual aspects that arise from changing the metal ion is difficult. Differences in ionic bond character between the metal and the formate anion can lead to differing electron density around the oxygen atoms, which serve as hydrogenbond acceptors.8 Varying ionic radii leads to differences in ReO<sub>3</sub>-network cavity size, which had been proposed to play an essential role in the phase transitions of zinc and magnesium analogues, DMZnF and DMMgF, and why no ordering occurs in the cadmium formate, DMCdF.21 Void dimensions also appear to play a role in the case of the Jahn-Teller distorted DMCuF.<sup>1,22</sup> Framework compressibility and flexibility are other factors that vary as a function of metal ion identity,<sup>23</sup> yet the contributions they make to the order-disorder transition temperature at ambient pressure have not been completely elucidated.

Changes in alkylammonium cation also dramatically affect the phase transition yet suffer similar limitations in terms of disentangling multiple influences. Changing the internal alkylammonium cation can lead to inequivalent structures due to the strong templating effect,<sup>24</sup> and alkylammonium ions are likely inhomogeneously distributed in mixed cation systems.<sup>25</sup> The number and strength of hydrogen bonds directly correlate to the temperature at which dynamic disorder sets in,<sup>26</sup> and replacement of hydrogen atoms with deuterium often leads to increases in transition temperature, as the deuterated hydrogen bond has greater polarity.<sup>4</sup> When dimethylammonium cobalt formate (DMCoF) is compared against its perdeutero counterpart (pd-DMCoF, [(CD<sub>3</sub>)<sub>2</sub>ND<sub>2</sub>]Co(DCOO)<sub>3</sub>), the paraelectric high-

temperature phase (HTP) is equivalent in the two analogues at room temperature. Upon cooling an order-disorder transition occurs at approximately the same temperature for both DMCoF and pd-DMCoF, although the low-temperature phase (LTP) of the two complexes differs. Furthermore, a third phase above room temperature is present in pd-DMCoF only. On the other hand, a negligible isotope effect was detected in DMZnF when nitrogen-15 is used.<sup>27</sup>

Although size effects are known to influence dielectric transitions, 16,28,29 very little work has been reported exploring reduced dimension particles of the alkylammonium metal formate family. Surfactant mediated mesoscale particles of DMZnF and methylammonium nickel formate (MANiF) have been generated as synthetic precursors ZnO and NiS porous materials, respectively, 30,31 although the role of size reduction or the influence of the PVP passivating layer on the order-disorder transition were not investigated. Averback<sup>32</sup> was able to synthesize micron and submicron-sized particles of some ammonium metal formates, AmMF,  $(M^{2+} = Ni, Mn, Zn, Co)$ . The structural phase transition appears to remain unchanged in AmNiF particles down to 300 nm. Similarly, for micron-sized particles of AmMnF no changes in transition temperature were detected. Abhyankar et al. 10 reported particle sets of the manganese analogue, DMMnF, generated by microwave synthesis with the smallest having a median edge length of  $2 \pm 1 \mu m$ . The authors noted a decrease in Curie temperature with decreasing particle size, with no ferroelectricity detected in particles below  $8\,\mu m$ . These observations were attributed to surface depolarization effects, although accompanying changes to the associated structural phase transition, if present, were not reported.

The present work seeks to further develop the synthetic means of achieving mesoscale particles without the need for surface stabilizers. Working with [(CH<sub>3</sub>)<sub>2</sub>NH<sub>2</sub>]Mg(HCOO)<sub>3</sub>, particles of 2.3 µm, 0.8 µm, 400 nm, and 200 nm were achieved, the smallest particle size being an order of magnitude smaller than any other reported in the DMMF family. The synthetic routes should complement other studies that use these materials as synthetic precursors to metal oxides,31 or studies on the influence of reduced particle size on dielectric or magnetic properties.<sup>10</sup> However, in addition, we use this series to examine the structural aspects of the order-disorder phase transition in DMMgF. Although at this size regime spontaneous polarization is not detectable, the metal-formate structural distortion is still present and shows particle size dependence, implicating the framework distortion as the determining factor of the order-disorder transition temperature in this member of the DMMF series.

#### **METHODS**

#### Materials Preparation

Magnesium(II) chloride hexahydrate, 88% formic acid, 200-proof ethanol, and *N,N*-dimethylformamide (DMF) were all purchased from Fisher Scientific; 40% dimethylamine solution in water and 98% 1-octyl-2-pyrrolidone were purchased from MilliporeSigma. All reagents were used without further purification.

[(CH<sub>3</sub>)<sub>2</sub>NH<sub>2</sub>]Mg(HCOO)<sub>3</sub> bulk crystals (1-B). Samples were synthesized using a method described by Jain et al.3 In a typical experiment, MgCl<sub>2</sub>·6H<sub>2</sub>O (1.917 mmol; 83 mM) was dissolved in a 23 mL 1:1 (v/v) mixture of water and DMF. The solution was sealed in a glass pressure vessel and heated to 140°C for three days under autogenous pressure. After being air-cooled to room temperature, the supernatant solution was decanted and crystallized through the slow evaporation of the solvent. After one week, the crystals were filtered and washed with ethanol. Colorless cubeshaped crystals were obtained. IR(KBr): ( $\nu NH_2$ ) Lit. = 2796 cm<sup>-1</sup>, Exp. = 2800 cm<sup>-1</sup>; (s,  $\nu$ HCOO<sup>-</sup>) Lit. = 1612 cm<sup>-1</sup>, Exp. =  $1608 \text{ cm}^{-1}$ ; (vCNC) Lit. =  $1026 \text{ cm}^{-1}$ , Exp. =  $1026 \text{ cm}^{-1}$ . TGA, Anal. Calcd: 44.6% loss ~460 K. Found: 44.4% loss PXRD: (012) Lit. =  $14.8^{\circ}$ , Exp. =  $14.7^{\circ}$ ; (-123) Lit. =  $24.8^{\circ}$ , Exp. = 24.8°; (-135) Lit. = 39.2°, Exp. =  $39.1^{\circ}$ .33

[(CH<sub>3</sub>)<sub>2</sub>NH<sub>2</sub>]Mg(HCOO)<sub>3</sub>particles (1-2.3)Mesoscale particles with an average size of 2.3  $\mu$ m  $\pm$  0.4  $\mu$ m were synthesized via direct addition of precursors. A 13 mL solution of 0.2168 g MgCl<sub>2</sub>·6H<sub>2</sub>O (1.07 mmol; 82.0 mM) in 200-proof ethanol was prepared. A second solution of 7 mL of ethanol with 135.2 μL 88% formic acid and 422 μL 40% aqueous dimethylamine solution was also prepared. The formic acid/dimethylamine solution was then directly added to the magnesium solution under magnetic stirring and capped. The solution was allowed to mature for 4 hours and then the suspended product was pipetted off. The solid was collected via centrifugation conducted at 9,400 RCF for 10 minutes. The particles were gently resuspended and washed twice with 40 mL DMF. Samples were dried under vacuum for 4 hours and then immediately used for calorimetry experiments. White crystalline powder (63% yield) IR(KBr):  $(vNH_2)$  Lit. = 2796 cm<sup>-1</sup>, Exp. = 2798 cm<sup>-1</sup>; (s, vH-COO<sup>-</sup>) Lit. = 1612 cm<sup>-1</sup>, Exp. = 1608 cm<sup>-1</sup>; (vCNC) Lit. = 1026 cm<sup>-1</sup>, Exp. =  $1026 \text{ cm}^{-1}$ .<sup>21</sup> TGA, Anal. Calcd:  $44.6\% \text{ loss} \sim 460$ K. Found: 43.5% loss. PXRD: (012) Lit. = 14.8°, Exp. = 14.7°; (-123) Lit. = 24.8°, Exp. = 24.7°; (-135) Lit. = 39.2°, Exp. =  $39.1^{\circ}.33$ 

 $[(CH_3)_2NH_2]Mg(HCOO)_3$  particles (1-0.8 µm). The 770 ± 190 nm sample was synthesized in a similar matter to 1-**2.3 µm** with a few exceptions: cold solvent was used during the mixing; the solution was allowed to warm up to room temperature naturally during the crystallization process; the reaction was scaled up by 7.5 times, and maturation time was extended to 17 hours. Most importantly, the sample was size selected for particles of a narrow size regime via differential centrifugation, resulting in a lower yield. Differential pelleting was applied to remove particles that pelleted under 625 RCF for 10 minutes twice and to remove particles that remained in suspension under 1000 RCF for 10 minutes twice. After each differential separation step, samples were redispersed in DMF and sonicated for 1 minute. White crystalline powder (4% yield). IR(KBr): ( $vNH_2$ ) Lit. =  $2796 \text{ cm}^{-1}$ , Exp. =  $2798 \text{ cm}^{-1}$ ; (s. vHCOO-) Lit. = 1612cm<sup>-1</sup>, Exp. =  $1609 \text{ cm}^{-1}$ ; (vCNC) Lit. =  $1026 \text{ cm}^{-1}$ , Exp. =  $1026 \text{ cm}^{-1}$  $cm^{-1}$ .<sup>21</sup> TGA, Anal. Calcd: 44.6% loss ~460 K. Found: 44.4% loss. PXRD: (012) Lit. = 14.8°, Exp. = 14.8°; (-123) Lit. = 24.8°, Exp. = 24.8°; (-135) Lit. = 39.2°, Exp. =  $39.2^{\circ}$ . 33

[(CH<sub>3</sub>)<sub>2</sub>NH<sub>2</sub>]Mg(HCOO)<sub>3</sub> particles (1-0.4  $\mu$ m). Particles with an average size of 380  $\pm$  180 nm were synthesized via

direct addition of precursors. A 13 mL solution of 0.2168 g MgCl<sub>2</sub>·6H<sub>2</sub>O (1.07 mmol; 82.0 mM) in DMF was prepared. A second solution of 7 mL of DMF with 135.2 µL 88% formic acid and 337.6 µL 40% aqueous dimethylamine solution was also prepared. The formic acid/dimethylamine solution was then directly added to the magnesium solution under magnetic stirring and capped. The solution was allowed to mature for 75 minutes, and then the suspended product was pipetted off. The solid was collected via centrifugation conducted at 9,400 RCF for 10 minutes. The particles were gently resuspended and washed twice with 40 mL DMF. Samples were dried under vacuum for 4 hours and then immediately used for calorimetry experiments. White crystalline powder (60.% yield). IR(KBr):  $(vNH_2)$  Lit. = 2796 cm<sup>-1</sup>, Exp. =  $2796 \text{ cm}^{-1}$ ; (s, vHCOO-) Lit. =  $1612 \text{ cm}^{-1}$ , Exp. = 1608cm<sup>-1</sup>; (vCNC) Lit. =  $1026 \text{ cm}^{-1}$ , Exp. =  $1026 \text{ cm}^{-1}$ .<sup>21</sup> TGA, Anal. Calcd: 44.6% loss ~460 K. Found: 43.6% loss. PXRD: (012) Lit. =  $14.8^{\circ}$ , Exp. =  $14.7^{\circ}$ ; (-123) Lit. =  $24.8^{\circ}$ , Exp. =  $24.8^{\circ}$ ; (-135) Lit. = 39.2°, Exp. = 39.1°.33

[(CH<sub>3</sub>)<sub>2</sub>NH<sub>2</sub>]Mg(HCOO)<sub>3</sub> particles (1-0.2  $\mu$ m). The 180 ± 40 nm sample was synthesized in a similar matter to 1-**0.4** μm with the following modifications: the reaction was scaled up by 7.5 times and maturation time was extended to 17 hours. Most importantly, the sample was size selected for particles of a narrow size regime via differential centrifugation, resulting in a lower yield. Differential pelleting was applied to remove particles that pelleted under 500 RCF for 10 minutes twice and to remove particles that remained in suspension under 875 RCF for 10 minutes twice. After each differential separation step, samples were redispersed in DMF and sonicated for 1 minute. White crystalline powder (11% yield). IR(KBr):  $(vNH_2)$  Lit. = 2796 cm<sup>-1</sup>, Exp. = 2798 cm<sup>-1</sup>; (s, vHCOO<sup>-</sup>) Lit. = 1612 cm<sup>-1</sup>, Exp. = 1610 cm<sup>-1</sup>; (vCNC) Lit. = 1026 cm<sup>-1</sup>, Exp. = 1026 cm<sup>-1</sup>.<sup>21</sup> TGA, Anal. Calcd: 44.6% loss ~460 K. Found: 44.5% loss. PXRD: (012) Lit. =  $14.8^{\circ}$ , Exp. =  $14.8^{\circ}$ ; (-123) Lit. =  $24.8^{\circ}$ , Exp. =  $24.8^{\circ}$ ; (-135) Lit. =  $39.2^{\circ}$ , Exp. =  $39.1^{\circ}$ .

Aliquots of  $[(CH_3)_2NH_2]Mg(HCOO)_3$  $Mg(HCOO)_2(H_2O)_2$  mixed crystalline powder (1'), taken while monitoring the reaction progress. Employing the direct addition of precursors, a 13 mL solution of 0.2168 g MgCl<sub>2</sub>·6H<sub>2</sub>O (1.07 mmol; 82.0 mM) in 200-proof ethanol was prepared. A second solution of 7 mL of ethanol with 135.2 μL 88% formic acid and 380 μL 40% aqueous dimethylamine solution was also prepared. The formic acid/dimethylamine solution was then directly added to the magnesium solution under magnetic stirring and capped. The solution was allowed to mature, pipetting off aliquots of the suspended product at 60 minutes, 80 minutes, 120 minutes, 5 hours, and 8 hours. Product was collected via centrifugation conducted at 9,400 RCF for 10 minutes. The particles were gently resuspended and washed once with 10 mL EtOH. Samples were dried overnight and then under vacuum two hours prior to thermal analysis.

(1' – 60 min). White Crystalline Powder. IR(KBr): (vOH) Lit. = 3380 cm<sup>-1</sup>, Exp. = 3386 cm<sup>-1</sup>; (s, vHCOO<sup>-</sup>) Lit. = 1600 cm<sup>-1</sup>, Exp. = 1603 cm<sup>-1</sup>; (δCH) Lit. = 1393 cm<sup>-1</sup>, Exp. = 1395 cm<sup>-1</sup>.<sup>34</sup> TGA, Anal. Calcd: 24.0% loss ~420 K. Found: 24.6% loss.<sup>33</sup> PXRD: (-1-11) Lit. = 18.0°, Exp. = 18.0°; (112) Lit. = 26.2°, Exp. = 26.2°; (113) Lit. = 34.4°, Exp. = 34.5°.<sup>33</sup>

(1' – 80 min). White Crystalline Powder. IR(KBr): (v0H) Lit. = 3380 cm<sup>-1</sup>, Exp. = 3389 cm<sup>-1</sup>; (s, vHCOO<sup>-</sup>) Lit. = 1600 cm<sup>-1</sup>, Exp. = 1603 cm<sup>-1</sup>; ( $\delta$ CH) Lit. = 1393 cm<sup>-1</sup>, Exp. = 1398 cm<sup>-1</sup>, <sup>34</sup> TGA, Anal. Calcd: 24.0% loss ~420 K. Found: 13.6% loss. <sup>33</sup> PXRD: (-1-11) Lit. = 18.0°, Exp. = 18.2°; (112) Lit. = 26.2°, Exp. = 26.4°; (113) Lit. = 34.4°, Exp. = 34.7°. <sup>33</sup>

(1' - 120 min). White crystalline powder. IR(KBr):  $(\nu NH_2)$  Lit. = 2796 cm<sup>-1</sup>, Exp. = 2798 cm<sup>-1</sup>; (s,  $\nu HCOO^-$ ) Lit. = 1612 cm<sup>-1</sup>, Exp. = 1607 cm<sup>-1</sup>; ( $\nu CNC$ ) Lit. = 1026 cm<sup>-1</sup>, Exp. = 1026 cm<sup>-1</sup>, 21 TGA, Anal. Calcd: 44.6% loss ~460 K. Found: 35.2% loss.<sup>33</sup> PXRD: (012) Lit. = 14.8°, Exp. = 14.8°; (-123) Lit. = 24.8°, Exp. = 24.8°; (-135) Lit. = 39.2°, Exp. = 39.2°, 33

(1' – 5 hrs). White crystalline powder. IR(KBr): ( $\nu$ NH<sub>2</sub>) Lit. = 2796 cm<sup>-1</sup>, Exp. = 2799 cm<sup>-1</sup>; (s,  $\nu$ HCOO<sup>-</sup>) Lit. = 1612 cm<sup>-1</sup>, Exp. = 1607 cm<sup>-1</sup>; ( $\nu$ CNC) Lit. = 1026 cm<sup>-1</sup>, Exp. = 1026 cm<sup>-1</sup>.<sup>21</sup> TGA, Anal. Calcd: 44.6% loss ~460 K. Found: 40.4% loss.<sup>33</sup> PXRD: (012) Lit. = 14.8°, Exp. = 14.8°; (-123) Lit. = 24.8°, Exp. = 24.8°; (-135) Lit. = 39.2°, Exp. = 39.2°.<sup>33</sup>

(1' – 8 hrs). White crystalline powder. IR(KBr): ( $\nu$ NH<sub>2</sub>) Lit. = 2796 cm<sup>-1</sup>, Exp. = 2798 cm<sup>-1</sup>; (s,  $\nu$ HCOO<sup>-</sup>) Lit. = 1612 cm<sup>-1</sup>, Exp. = 1607 cm<sup>-1</sup>; ( $\nu$ CNC) Lit. = 1026 cm<sup>-1</sup>, Exp. = 1026 cm<sup>-1</sup>, 2<sup>1</sup> TGA, Anal. Calcd: 44.6% loss ~460 K. Found: 41.2% loss.<sup>33</sup> PXRD: (012) Lit. = 14.8°, Exp. = 14.9°; (-123) Lit. = 24.8°, Exp. = 25.0°; (-135) Lit. = 39.2°, Exp. = 39.3°.<sup>33</sup>

#### **Characterization Methods**

Transmission electron microscopy (TEM) was performed using a Hitachi H-7000 equipped with a Veleta (2 k X 2k) CCD side mount camera operated at 100 kV. Samples were prepared by adding dropwise 40 µL of the product resuspended in 20 mL DMF solution that had been treated with 40 μL of 1-octyl-2-pyrrolidone to help prevent the aggregation or fusion of particles upon drying. The grids were 400mesh copper with a carbon support film from Ted-Pella, Inc. Grids were allowed to dry in air overnight, then vacuumdried for a minimum of two hours. Particle size was measured for 75-300 particles from various areas on the sample grid using ImageJ imaging software.35 Scanning electron microscopy (SEM) was performed on FEI Nova NanoSEM 430 operated at 15 kV. Samples were ground, affixed to the mounting peg using carbon tape, and coated with ~10 nm of Au-Pd before image collection. Particle size was measured for approximately 100 particles using ImageJ imaging software from various areas on the sample grid.35 When determining particle sizes with TEM or SEM, **1-2.3 μm** and **1-0.8 μm** were cubic, so the edge length was measured and reported, whereas 1-0.4 μm and 1-0.2 μm have ill-defined shapes, so the particle length was approximated by using the square root of the measured particle area.

Differential Scanning Calorimetry (DSC) was performed on a TA Instruments Q1000 calorimeter using hermetic aluminum pans purged under helium gas at 25 mL/min. Approximately 3 mg of freshly dried sample was weighed on an analytical balance immediately after the 4-hour drying. The sample was then loaded into the pan, the pan was crimped and introduced using an automated sample loader. Data were collected at 2 K/min and 10 K/min. The transition temperature was determined by finding the midway point between the endothermic and exothermic peak maxima. The thermal hysteresis was determined by finding the

difference between the endothermic and exothermic peak maxima.

Thermal gravimetric analysis (TGA) was performed on a Perkin-Elmer TGA 7 Thermogravimetric analyzer at a heating rate of 5 K/min under nitrogen purge flow at 10 mL/min. Ambient Powder X-ray diffraction (PXRD) measurements were carried out on a Panalytical X'Pert Powder diffractometer using CuK $\alpha$  radiation ( $\lambda=1.54056$  Å). Ground samples of approximately 20 mg were mounted on a glass slide with double-sided tape and placed on a flat sample support. Fourier transform infrared (FTIR) spectroscopy was performed with a Nicolet 6700 Thermo Scientific spectrophotometer. The spectral window was between 4000 cm $^{-1}$  and 400 cm $^{-1}$  and samples were prepared by grinding about 1 mg of sample into 300 mg of dry KBr.

Variable Temperature Powder X-ray diffraction (VT-PXRD) measurements were carried out on a Bruker DUO diffractometer. An IµS power source with multi-layered mirror optics provided Cu K $\alpha$  radiation ( $\lambda$  = 1.54178 Å), which was detected by an APEXII CCD area detector (1024  $\times$  1024 detection format). The samples were loaded into a 0.3 mm (ID) thin-walled boron enriched capillaries from the Charles Supper Company and placed 150 mm away from the detector. Diffraction patterns were collected at 300 K and 100 K between 5 and 60° 20.

Dielectric measurements were performed on a powder pellet. The pellet was formed through drying and was not pressed. A silver paint with n-butylacetate was applied to two flat opposite sides of the pellet to the geometry of a parallel plate capacitor. An Andeen-Hagerling AH2700A capacitance bridge was employed at frequencies ranging from 0.1-20 kHz. The dielectric constant was then obtained from the capacitance measurement and pellet geometry.

The polarization was obtained by integrating the pyroelectric current with respect to time. For the pyroelectric current measurement, the sample was first cooled down through the transition temperature under electric field. Then the electric field was removed, and the transient current was measured with a Keithley 6517 electrometer upon warming.

#### **RESULTS**

#### Synthesis of Small Particles

Size and Shape. Four sets of mesoscale particles of 1 with different sizes were prepared via the direct addition of precursors, Figure 1. The particle sizes of the sets range from  $2.3 \pm 0.4 \, \mu m$  down to  $180 \pm 40$  nm, as summarized in Table 1, and the four separate samples will be referred to throughout the manuscript by their average particle size, 1-2.3 μm, 1-0.8 μm, 1-0.4 μm and 1-0.2 μm. Particles were measured using SEM, and histograms of the particle size measurements are provided in Figure S1. The larger particles have the characteristic cubic shape,  $^{2,3,8,10,30-33,36}$  while particles sets 1-0.4 μm and 1-0.2 μm are less regular.

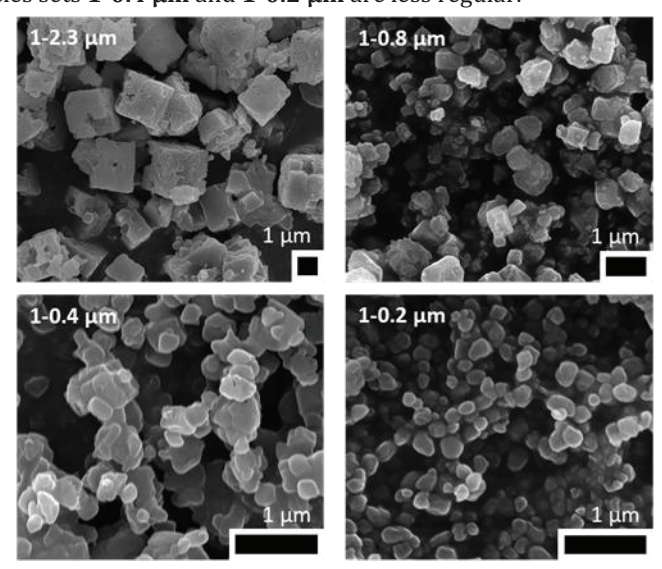


Figure 1. SEM images of particles from samples 1-2.3  $\mu$ m, 1-0.8  $\mu$ m, 1-0.4  $\mu$ m, 1-0.2  $\mu$ m.

**Method of Synthesis.** Although dimethylammonium metal formates are typically prepared beginning with solvothermal generation of formic acid and dimethylamine, <sup>1,2</sup> the direct addition of precursors affords better control of synthetic parameters. Additionally, thermally generated impurities created during the solvothermal process<sup>37</sup> can be avoided. The reagent concentrations reported by Pato-Doldán et al.<sup>8,38</sup> for the solvent layering synthesis of **1** pro-

Table 1. Transition temperatures, a thermal hysteresis, and transition enthalpy and entropy as measured by DSC.d

Size	Sample	<i>T</i> <sub>c</sub> (K)	Hysteresis (K)	ΔH (kJ/mol)	ΔS (J mol <sup>-1</sup> K <sup>-1</sup> )
Bulk	Theoretical <sup>8</sup>			2.44	9.13
Bulk	Asaji et al. <sup>38</sup>	263		2.7±0.2	10±1
Bulk	1-B	263.4	5.5	2.82	10.59
2.3±0.4 μm	1-2.3 μm	259.9±0.1	8.4±0.6	2.20±0.06	8.34±0.25
770±190 nm	1-0.8 μm	258.4	15.6	1.55	5.82
380±180 nm	1-0.4 μm	251.5±0.1	13.0±1.1	1.09±0.03	4.23±0.12
180±40 nm	1-0.2 μm	251.0	18.5	1.02	3.92

<sup>&</sup>lt;sup>a</sup>The transition temperature, *T*<sub>c</sub>, is defined as the halfway point between the endothermic and exothermic peak maxima.

bThe hysteresis is the difference between the endothermic and exothermic peak maxima.

<sup>&</sup>lt;sup>c</sup>Enthalpy and entropy were measured for the endothermic peak maxima.

dAll values use a ramp rate of 10 K/min, including data from Asaji et al.38 and Pato-Doldán et al.8

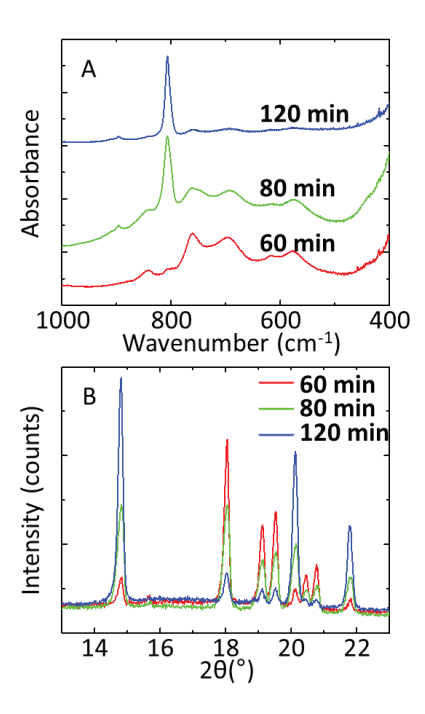


**Figure 2.** FTIR (A) and PXRD (B) monitoring the reaction progress during the synthesis of DMMgF sample **1'** described in the Experimental Section, with aliquots collected at maturation times of 60 minutes, 80 minutes, and 120 minutes. In A, the symmetric carboxylate bending mode is followed. The peak at 807 cm<sup>-1</sup>, characteristic of DMMgF,<sup>21</sup> emerges while the peak at 761 cm<sup>-1</sup>, characteristic of MgFDH,<sup>34</sup> recedes. In B, reflections at 14.8° (012), 20.1° (-114), and 21.8 (-120) emerge over time and are characteristic of DMMgF,<sup>33</sup> while the receding reflections at 15.6° (011), 18.0° (-1-11), 19.1° (002), 19.5 (111), 20.4 (-102), and 20.7 (200) are characteristic of MgFDH.<sup>33</sup>

vided the starting point for the particle syntheses reported here. Although surfactants are sometimes used to isolate discrete particles of the formate networks,<sup>30</sup> they were not used in the present work to avoid their impact on solid-state properties, which at the mesoscale can be altered by surface modification,<sup>39-45</sup> and with an eye toward further work incorporating the particles into heterostructures.

Metal formate kinetic products, 10,32,37 in the present case magnesium formate dihydrate, MgFDH, complicate traditional approaches for isolating small particles of 1 and other metal formate perovskites. For example, attempts to form small particles by forcing rapid precipitation early in the growth process results in significant levels of the MgFDH side product, as discussed further, below. In general, the mesoscale particles of 1 were achieved by determining adequate maturation time to consume the initially formed MgFDH while minimizing ripening of the product by harvesting samples as soon as fully mature. Chemical variations, including reducing water content, also limited side products and different synthetic conditions helped target different particle sizes. Larger micron-sized particles were isolated when using ethanol as the solvent, while particles in the hundreds of nanometers were achieved in N,N-dimethylformamide (DMF) when reducing the amount of excess dimethylamine.

Minimizing Metal Formate Dihydrate. The presence of metal formate dihydrates, M(HCOO)<sub>2</sub>(H<sub>2</sub>O)<sub>2</sub> (MFDH), as side products is common during synthesis of the formate perovskites, for example appearing in reports on dimethylammonium cobalt formate<sup>37</sup> and dimethylammonium manganese formate, 10 as well as during the synthesis of ammonium nickel formate.32 Generally, strategies to grow small inorganic particles typically involve rapid formation of multiple crystallite nuclei and abbreviated maturation times, but there are limitations to prematurely terminating particle growth in the present system As seen in Figures 2 and S4, the relative intensities of IR signatures of 1 and MgFDH depend on maturation time and sample handling. TGA (Figure S5) is the preferred method to quantify the MgFDH content of products, and Figure 3a shows samples harvested soon after precipitation consisted of MgFDH, but as reactions progressed, the signals representative of 1 begin to predominate, eventually reaching an equilibrium. The rate<sup>32,37</sup> and overall completeness of the transformation depends on several factors, including solvent and the reagent ratio, as shown in Figure 3b. The conversion from MgFDH to 1 in the reactions reported here occurs in hours to days.

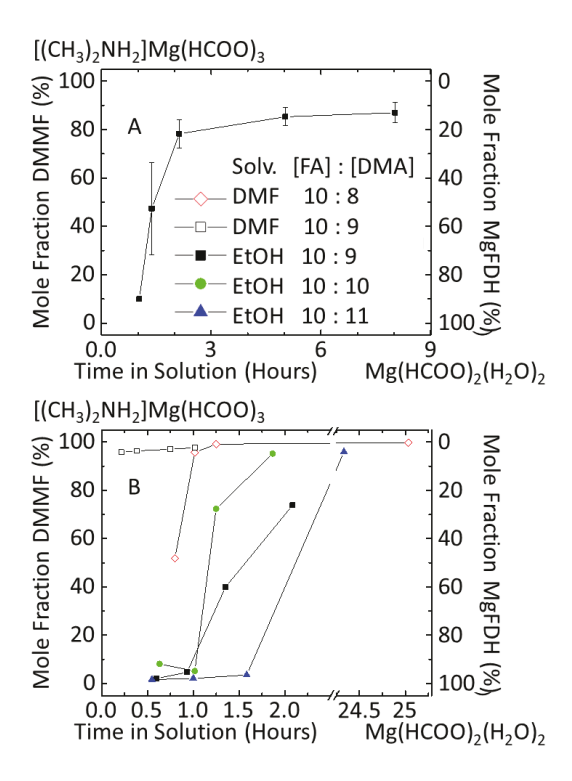


**Figure 3.** Mole fraction of DMMgF and or MgFDH relative to the mixed product as a function of maturation time for different synthetic conditions. (A) Monitoring the reaction of sample 1', described in the experimental section. (B) Monitoring different synthetic conditions. The relative amounts of MgFDH and DMMgF were determined by thermogravimetric analysis performed at a heating rate of 5 K/min under nitrogen purge flow at 10 mL/min.

**Limiting Polydispersity.** Generally, synthetic attempts in the absence of surfactants led to polydisperse samples, requiring differential centrifugation to reduce the particle size dispersion. Sample sets  $1-0.8~\mu m$  and  $1-0.2~\mu m$  were

isolated in this way, greatly reducing the product yield. On the other hand, the 1-2.3 µm and 1-0.4 µm sample sets did not require post-synthetic size selection. By adjusting the concentrations of the dimethylamine reagent relative to the metal ion and formic acid, narrower size dispersions could be achieved. The larger particles, **1-2.3 μm**, were achieved using ethanol as the crystallization solvent, allowing the particles to mature for a longer time, and having an equivalent concentration of dimethylamine and formic acid. Smaller particles, **1-0.4 μm**, were achieved using DMF as the crystallization solvent, having shorter maturation time, and reducing the excess dimethylamine used in the synthesis. The **1-0.8 μm** and **1-0.2 μm** particle sizes were achieved with the synthetic procedures of 1-2.3 μm and 1-0.4 μm, respectively, and extending the maturation time to allow for Ostwald ripening to give a more polydisperse sample set. The target particle sizes were then selectively harvested from the polydisperse sample set via differential centrifuga-

## Investigations into Size Effects on the Order-disorder Transitions

Dielectric and Polarization Measurements. The dielectric response of particle samples 1-0.8  $\mu m$  and 1-0.2  $\mu m$  are compared to that of the bulk crystals, referred to as 1-B in Figure 4. For each sample there is a clear transition in the

vicinity of 260 K, which for the bulk corresponds to the order-disorder phase transition, although the transition temperature decreases slightly for the mesoscale particles. The inflection point of the warming curve occurs at 264 K in 1-B, while it occurs at 258 K and 248 K for 1-0.8 µm and 1-0.2 μm, respectively. The onset of the transition is also more gradual in the particles compared to the response of the bulk sample, attributable to the polydispersity and associated variable coherence length inherent to particle samples. 46 Below the transition onset the signal is characterized by a broad frequency-dependent response between 150 and 250 K, previously observed for 1.7,8 A similar response is retained in the particle samples. The frequency dependence of the imaginary dielectric permittivity can be used to determine the activation energy of the dipolar process, as seen in Figure S6. The activation energy for the bulk sample is slightly larger than that of the reduced particle samples, however all the measurements have a value of about 300 meV, in line with previous estimates.<sup>47</sup>

The polarization of **1-B** was confirmed below 260 K in a pyroelectric measurement, Figure S7 and Figure S8. On the other hand, no pyroelectric effect was detected for the particle samples **1-0.8**  $\mu m$  and **1-0.2**  $\mu m$ , indicating either the polarization is too weak to detect or is absent. The absence of polarization would be consistent with the earlier study of Abhyankar et al. <sup>10</sup> on size reduced

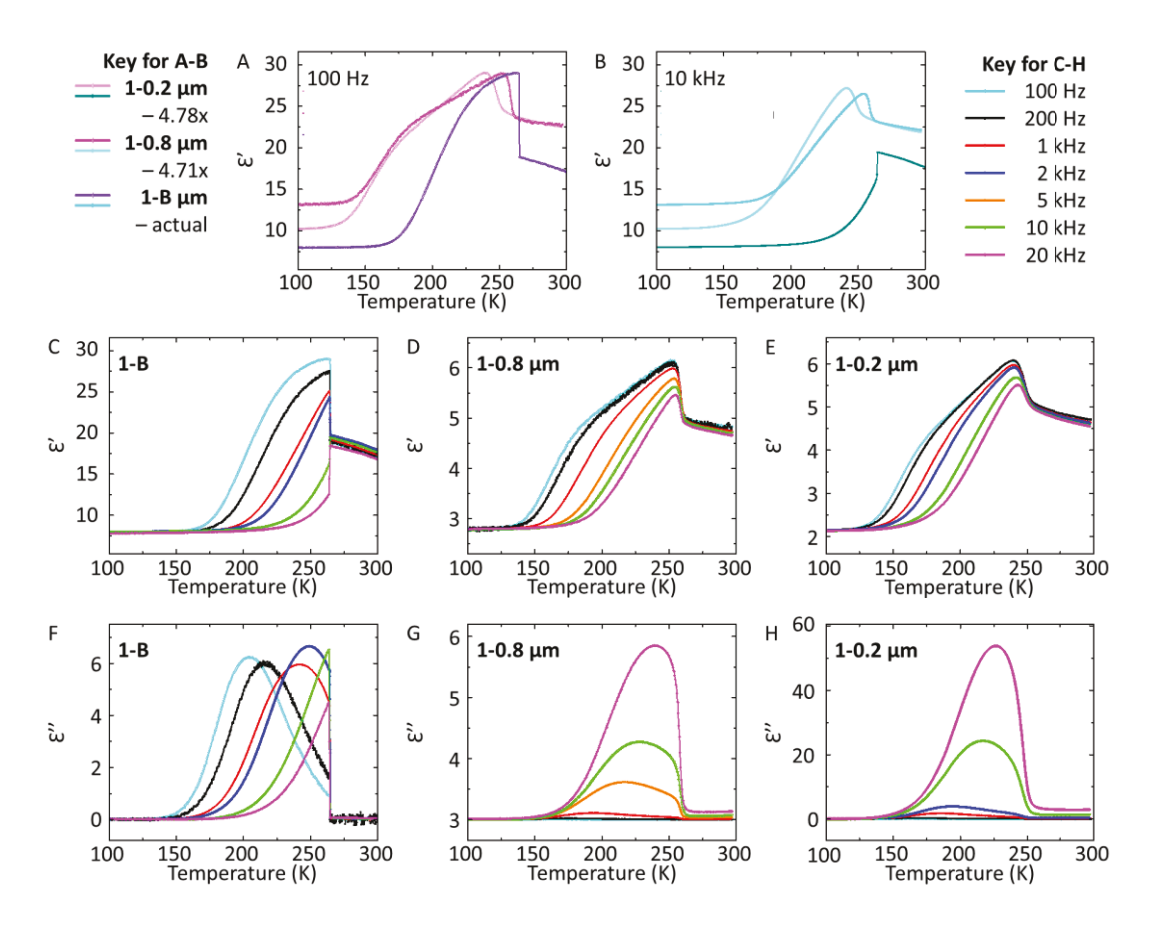
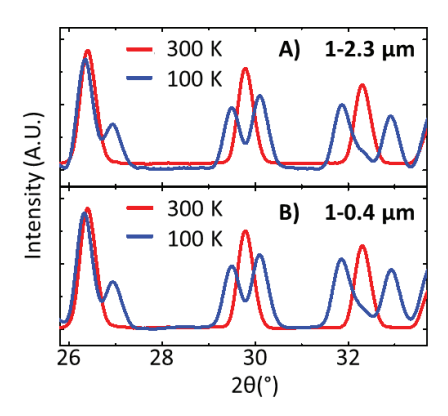


Figure 4. Dielectric constant measurements for samples of 1 measured upon warming at 2 K/min. The real component of the dielectric constant of 1-B, 1-0.8 μm, and 1-0.2 μm measured at 100 Hz (A) and at 10 kHz (B). The real and imaginary components of the dielectric constant of 1-B (C and D) 1-0.8 μm (E and F) and 1-0.2 μm (G and H) measured at different frequencies.



**Figure 5.** VT-PXRD patterns for (A) **1-2.3**  $\mu$ m and (B) **1-0.4**  $\mu$ m. Patterns collected at 300 K (red) are consistent with the paraelectric HTP of **1**, while the patterns collected at 100 K (blue) are consistent with the known LTP.<sup>8</sup> Peak assignments are tabulated in the SI.

particles of DMMnF, which concluded ferroelectricity was suppressed at particle sizes below 8  $\mu m.$ 

The similarity of the phase transition seen in the vicinity of 260 K for the bulk as well as particle samples was confirmed using powder X-ray diffraction of **1-B**, **1-2.3**  $\mu$ m and **1-0.4**  $\mu$ m, above the transition temperature at 300 K and below at 100 K, Figure 5. The high-temperature patterns can be indexed to the *R-3c* space group of the reported high-temperature structure, and symmetry lowering, consistent with the known order-disorder transition of **1**, is observed at 100 K for all samples.<sup>8,20,33</sup> While the structure of the low-temperature phase has not been solved for **1**, Pato-Doldán et al have attributed the LTP to the non-centrosymmetric space group, Cc,<sup>8</sup> with C2/c also a possible assignment,<sup>48</sup> the PXRD study demonstrates the mesoscale particles **1-2.3**  $\mu$ m and **1-0.4**  $\mu$ m undergo the same structural transition as the bulk material.

**DSC Measurements of the Phase Transition.** The dielectric measurements show a lowering of the phase transition temperature as particles become smaller and this effect was interrogated further with differential scanning calorimetry (DSC), Figure 6, Figure S9, and Figure S10. The  $T_{\rm c}$ , defined as the halfway point between the endothermic and exothermic peak maxima, for **1-B** is 263 K, consistent with earlier reports.<sup>38</sup> For the particle samples,  $T_{\rm c}$  continuously decreases as the particles get smaller, observed at 260 K for **1-2.3 \mum**, 258 K for **1-0.8 \mum**, 252 for **1-0.4 \mum** and 251 K for **1-0.2 \mum**.

The enthalpy of the phase transition is also influenced by particle size, Table 1 and Figure S10. A value of  $\Delta H=2.8$  kJ/mol was measured for **1-B**, effectively reproducing the value of 2.7 kJ/mol reported by Asaji et al. For **1-2.3 \mum**, the enthalpy is slightly suppressed, having a value of 2.2 kJ/mol. As the particles become smaller, the enthalpy is further suppressed to 1.6 kJ/mol for **1-0.8 \mum**, 1.1 kJ/mol for **1-0.4 µm** and 1.0 kJ/mol for **1-0.2 µm**. A clear trend of decreasing enthalpy with decreasing particle size was observed, which can be attributed to the increased contribution of a disordered surface.  $^{49-56}$  Changes with particle size

are also apparent in the thermal hysteresis of the phase transition in DSC, Figure 6. The bulk crystals **1-B** had the smallest hysteresis of 5 K, which increased to 19 K for **1-0.2**  $\mu m$  when measured at a scan rate of 10 K/min. This trend was also seen at slower scan rates in Figure S9.

#### **DISCUSSION**

The lack of pyroelectric current in the submicron DMMgF particles is consistent with studies on the manganese analogue, DMMnF, by Abhyankar et al.  $^{10}\,$  These authors prepared particles as small as 2  $\mu m$  and reported the spontaneous polarization was suppressed as particle size decreased below the estimated domain wall thickness of 10  $\mu m$  in the

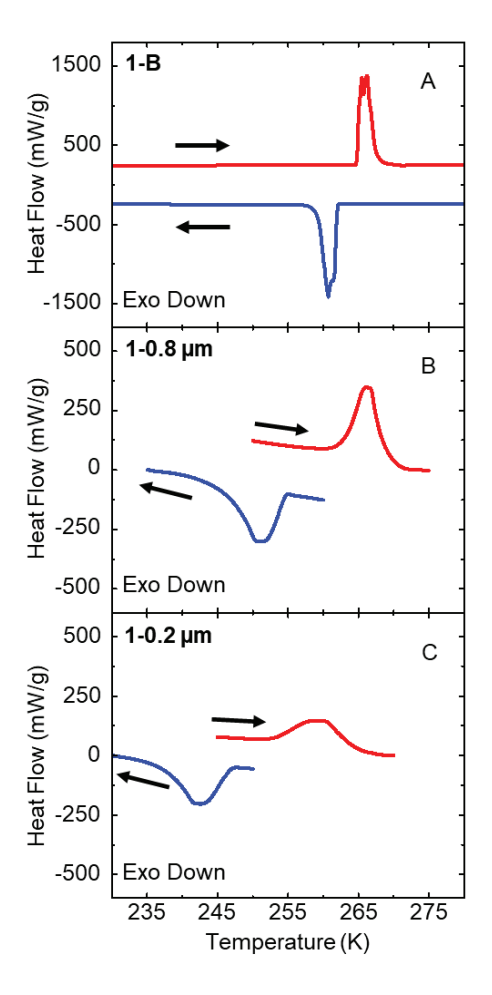


**Figure 6.** DSC curves for samples of DMMgF: (A) **1-B** (B) **1-0.8**  $\mu m$  and (C) **1-0.2**  $\mu m$ . The ramp rate is 10 K/min. Thermodynamic data derived from the scans appears in Table 1.

metal-organic perovskites.<sup>10</sup> Although polarization was measured in the bulk sample of **1-B**, all the particle samples prepared here are also well below the critical size anticipated to support spontaneous polarization. At the same time, while pyroelectricity is lost in the small particles, the structural phase change associated with the order-disorder transition in DMMgF is still present. Therefore, the particle size study sheds some light on the driving force for the phase change associated with the dielectric response of the bulk materials.

The change in transition temperature with particle size signals a change in the thermodynamic barrier, attributable to changing surface contribution to the total energy as the surface to volume ratio changes. The lowering of the transition temperature indicates stabilization of the high-volume high-temperature phase in smaller particles, behavior that is frequently seen in network solids, suggesting the high volume phase experiences lower surface energy. 57,58 Changes in ΔH of the transition, decreasing at smaller particle size, is also attributable to the enhanced surface contribution.<sup>59</sup> The thermal hysteresis seen in the DSC reflects the kinetic barrier and, for solid-solid phase transitions, the barrier is primarily elastic in nature, reflecting cooperative changes in framework bond lengths and bond angles.<sup>60</sup> For the particle samples, the hysteresis increases at smaller size reflecting an increase in the elastic barrier. First-order solid-solid phase transitions nucleate at defects, and it has been shown that as particles become smaller the number of nucleation sites decreases, increasing the kinetic barrier. 61 In the size regimes studied here, the thermal hysteresis in the DSC, measured at 2 K/min, changes from 2.75 K in the bulk sample to 18.5 K for the 180 nm particles, consistent with expectations. The maximum barrier is expected for the largest particle size containing a single nucleation site.61 Below this, the elastic barrier decreases toward the molecular limit. As the hysteresis width is largest for the smallest particles prepared in this study, it suggests 180 nm is still larger than the single nucleation site regime. However, the particle size dependence is consistent with expectations for an elastic contribution to the phase transition.

There are three general aspects to the order-disorder transition in the DMMF family of perovskites: ordering of the hydrogen bonding interactions between the dimethylammonium cations and the framework, deformation of the framework to better accommodate the hydrogen bonds. and long-range polarization. The influence of particle size on spontaneous polarization has already been described, 10 and our results support this earlier observation that it is not seen in sub-micron particles of the metal formates, a consequence of the relatively weak polarization in these solids. The studies on particles confirm, as is largely accepted by workers in this area,5,20,62-66 the ferroelectric response of these solids, when observed, is a byproduct of the cation ordering phase transition, which occurs even though the particles do not support polarization. While the hydrogen bonding is quite strong in these compounds,38,64 the interaction between a cation and the framework is relatively independent of the other cations,64 meaning this step alone does not have a significant elastic component and is not expected to be influenced by particle size. That leaves the framework deformation, sometimes referred to as framework collapse,11,64 as the aspect of the transition with an elastic contribution that still occurs in the particles and is subject to surface-to-volume effects. Therefore, the behavior of the mesoscale particles points to the framework deformation as the step that determines the phase transition temperature. This conclusion is in line recent explorations of other analogues, including studies analyzing the dipolar dynamics in DMZnF,7 total neutron scattering and modeling for DMMnF,64 and alterations to the phase transition under pressure, also of DMMnF.14,67

#### CONCLUSION

The counterion order-disorder transition in dimethylammonium magnesium formate is demonstrated to be sensitive to changes in the surface to volume ratio. While the solid-solid phase change is retained for micron and submicron particles, these reduced size particles do not possess a detectable pyroelectric current. The result parallels an earlier study on the manganese analogue which concluded surface depolarization effects restrict spontaneous polarization in micron-sized particles, a consequence of the relatively low electric polarization in this family. Nevertheless, the cation ordering occurs in the smaller particles, with the transition temperature decreasing as the larger surface to volume ratio stabilizes the high temperature phase. Additionally, the larger surface to volume ratio leads to a decrease in the enthalpy of the transition, reflecting the greater contribution of the less ordered surface. Analysis of the thermal hysteresis shows the smaller particles experience a larger elastic barrier to the phase change, which can be attributed to a reduction of the number of nucleation points from which the transition can propagate. These observations on how the phase transition changes with particle size signal it is the elastic barrier associated with the framework deformation that determines the transition temperature of the order-disorder transition in dimethylammonium magnesium formate. Finally, the study was enabled by new synthetic approaches to the mesoscale particles, which were produced without the aid of surfactants.

#### **ASSOCIATED CONTENT**

Further particle characterization, including particle size analysis, TEM images, PXRD, TGA, DSC and polarization measurements. This material is available free of charge via the Internet at http://pubs.acs.org.

#### **AUTHOR INFORMATION**

#### Corresponding Author

\* talham@chem.ufl.edu

#### **ACKNOWLEDGMENT**

We acknowledge the financial support by the National Science Foundation through grants DMR-1405439 and DMR-1904596. We thank the NSF for funding of the X-ray diffractometer through grant CHE-1828064. A portion of this work was performed at the National High Magnetic Field Laboratory, which is supported by the National Science Foundation Cooperative Agreement No. DMR-1644779 and the state of Florida.

#### **REFERENCES**

- (1) Sletten, E.; Jensen, L. H. The Crystal Structure of Dimethylammonium Copper(II) Formate, NH<sub>2</sub>(CH<sub>3</sub>)<sub>2</sub>[Cu(00CH)<sub>3</sub>]. *Acta Crystallogr., Sect. B: Struct. Crystallogr. Cryst. Chem.* **1973**, *29*, 1752-1756
- (2) Jain, P.; Dalal, N. S.; Toby, B. H.; Kroto, H. W.; Cheetham, A. K. Order-Disorder Antiferroelectric Phase Transition in a Hybrid Inorganic-Organic Framework with the Perovskite Architecture. *J. Am. Chem. Soc.* **2008**, *130*, 10450-10451.
- (3) Jain, P.; Ramachandran, V.; Clark, R. J.; Zhou, H. D.; Toby, B. H.; Dalal, N. S.; Kroto, H. W.; Cheetham, A. K. Multiferroic Behavior Associated with an Order-Disorder Hydrogen Bonding Transition

- in Metal-Organic Frameworks (MOFs) with the Perovskite ABX<sub>3</sub> Architecture. *J. Am. Chem. Soc.* **2009**, *131*, 13625-13627.
- (4) Fu, D.-W.; Zhang, W.; Cai, H.-L.; Zhang, Y.; Ge, J.-Z.; Xiong, R.-G.; Huang, S. D.; Nakamura, T. A Multiferroic Perdeutero Metal-Organic Framework. *Angew. Chem., Int. Ed.* **2011**, *50*, 11947-11951.
- (5) Šimėnas, M.; Kultaeva, A.; Balčiūnas, S.; Trzebiatowska, M.; Klose, D.; Jeschke, G.; Maczka, M.; Banys, J.; Pöppl, A. Single Crystal Electron Paramagnetic Resonance of Dimethylammonium and Ammonium Hybrid Formate Frameworks: Influence of External Electric Field. *J. Phys. Chem. C* **2017**, *121*, 16533-16540.
- (6) Xu, G.; Ma, X.; Zhang, L.; Wang, Z.; Gao, S. Disorder–Order Ferroelectric Transition in the Metal Formate Framework of [NH<sub>4</sub>][Zn(HCOO)<sub>3</sub>]. *J. Am. Chem. Soc.* **2010**, *132*, 9588–9590.
- (7) Šimėnas, M.; Balčiūnas, S.; Ciupa, A.; Vilčiauskas, L.; Jablonskas, D.; Kinka, M.; Sieradzki, A.; Samulionis, V.; Mączka, M.; Banys, J. Elucidation of Dipolar Dynamics and the Nature of Structural Phases in the [(CH<sub>3</sub>)<sub>2</sub>NH<sub>2</sub>][Zn(HCOO)<sub>3</sub>] Hybrid Perovskite Framework. *J. Mater. Chem. C* **2019**, *7*, 6779-6785.
- (8) Pato-Doldán, B.; Sánchez-Andújar, M.; Gómez-Aguirre, L. C.; Yáñez-Vilar, S.; López-Beceiro, J.; Gracia-Fernández, C.; Haghighirad, A. A.; Ritter, F.; Castro-García, S.; Señarís-Rodríguez, M. A. Near Room Temperature Dielectric Transition in the Perovskite Formate Framework [(CH<sub>3</sub>)<sub>2</sub>NH<sub>2</sub>][Mg(HCOO)<sub>3</sub>]. *Phys. Chem. Chem. Phys.* **2012**, *14*, 8498-8501.
- (9) Abhyankar, N.; Bertaina, S.; Dalal, N. S. On Mn<sup>2+</sup> EPR Probing of the Ferroelectric Transition and Absence of Magnetoelectric Coupling in Dimethylammonium Manganese Formate (CH<sub>3</sub>)<sub>2</sub>NH<sub>2</sub>Mn(HCOO)<sub>3</sub>, a Metal-Organic Complex with the Pb-Free Perovskite Framework. *J. Phys. Chem. C* **2015**, *119*, 28143-28147.
- (10) Abhyankar, N.; Lee, M.; Foley, M.; Choi, E. S.; Strouse, G.; Kroto, H. W.; Dalal, N. S. Efficient Synthesis and Tailoring of Magnetic and Dielectric Properties of Pb-Free Perovskite-Like ABX<sub>3</sub> Metal-Organic Frameworks. *Phys. Status Solidi RRL* **2016**, *10*, 600-605.
- (11) Abhyankar, N.; Kweon, J. J.; Orio, M.; Bertaina, S.; Lee, M.; Choi, E. S.; Fu, R. Q.; Dalal, N. S. Understanding Ferroelectricity in the Pb-Free Perovskite-Like Metal Organic Framework [(CH<sub>3</sub>)<sub>2</sub>NH<sub>2</sub>]Zn(HCOO)<sub>3</sub>: Dielectric, 2D NMR, and Theoretical Studies. *J. Phys. Chem. C* **2017**, *121*, 6314-6322.
- (12) Uchino, K. *Ferroelectric Devices*, 2<sup>nd</sup> ed.; CRC Press: Boca Raton, 2010; p 20.
- (13) Ionescu, A. M. Ferroelectric Devices Show Potential. *Nat. Nanotechnol.* **2012**, *7*, 83-85.
- (14) Xin, L.; Fan, Z.; Li, G.; Zhang, M.; Han, Y.; Wang, J.; Ong, K. P.; Qin, L.; Zheng, Y.; Lou, X. Growth of Centimeter-Sized [(CH<sub>3/2</sub>NH<sub>2</sub>]Mn(HCOO)<sub>3</sub> Hybrid Formate Perovskite Single Crystals and Raman Evidence of Pressure-Induced Phase Transitions. *New J. Chem.* **2017**, *41*, 151-159.
- (15) Janolin, P.-E. Strain on Ferroelectric Thin Films. *J. Mater. Sci.* **2009**, *44*, 5025-5048.
  - (16) Fridkin, V.; Ducharme, S. Ferroelectricity at the Nanoscale *Basics and Applications*; Springer: Heidelberg, 2014.
- (17) Martin, L. W.; Rappe, A. M. Thin-Film Ferroelectric Materials and their Applications. *Nat. Rev. Mater.* **2017**, *2*, 16087.
- (18) Wang, Z.; Zhang, B.; Otsuka, T.; Inoue, K.; Kobayashi, H.; Kurmoo, M. Anionic NaCl-Type Frameworks of [Mn<sup>II</sup>(HCOO)₃<sup>-</sup>], Templated by Alkylammonium, Exhibit Weak Ferromagnetism. *Dalton Trans.* **2004**, 2209-2216.
- (19) Sánchez-Andújar, M.; Presedo, S.; Yáñez-Vilar, S.; Castro-García, S.; Shamir, J.; Señarís-Rodríguez, M. A. Characterization of the Order-Disorder Dielectric Transition in the Hybrid Organic-Inorganic Perovskite-Like Formate Mn(HCOO)<sub>3</sub>[(CH<sub>3</sub>)<sub>2</sub>NH<sub>2</sub>]. *Inorg. Chem.* **2010**, *49*, 1510-1516.
- (20) Mączka, M.; Gągor, A.; Macalik, B.; Pikul, A.; Ptak, M.; Hanuza, J. Order-Disorder Transition and Weak Ferromagnetism in the Perovskite Metal Formate Frameworks of

- $[(CH_3)_2NH_2][M(HCOO)_3]$  and  $[(CH_3)_2ND_2][M(HCOO)_3]$  (M = Ni, Mn). Inorg. Chem. **2014**, 53, 457-467.
- (21) Szymborska-Malek, K.; Trzebiatowska-Gusowska, M.; Mączka, M.; Gągor, A. Temperature-Dependent IR and Raman Studies of Metal-Organic Frameworks [(CH<sub>3</sub>)<sub>2</sub>NH<sub>2</sub>][M(HCOO)<sub>3</sub>], M = Mg and Cd. *Spectrochim. Acta, Part A* **2016**, *159*, 35-41.
- (22) Wang, Z.; Jain, P.; Choi, K.-Y.; van Tol, J.; Cheetham, A. K.; Kroto, H. W.; Koo, H.-J.; Zhou, H.; Hwang, J.; Choi, E. S., et al. Dimethylammonium Copper Formate [(CH<sub>3</sub>)<sub>2</sub>NH<sub>2</sub>]Cu(HCOO)<sub>3</sub>: A Metal-Organic Framework with Quasi-One-Dimensional Antiferromagnetism and Magnetostriction. *Phys. Rev. B* **2013**, *87*, 224406.
- (23) Mączka, M.; da Silva, T. A.; Paraguassu, W.; da Silva, K. P. Raman Scattering Studies of Pressure-Induced Phase Transitions in Perovskite Formates [(CH<sub>3</sub>)<sub>2</sub>NH<sub>2</sub>]Mg(HCOO)<sub>3</sub> and [(CH<sub>3</sub>)<sub>2</sub>NH<sub>2</sub>]Cd(HCOO)<sub>3</sub>. Spectrochimica Acta Part a-Molecular and Biomolecular Spectroscopy **2016**, 156, 112-117.
- (24) Wang, Z.; Hu, K.; Gao, S.; Kobayashi, H. Formate-Based Magnetic Metal-Organic Frameworks Templated by Protonated Amines. *Adv. Mater.* **2010**, *22*, 1526-1533.
- (25) Chen, S.; Shang, R.; Wang, B. W.; Wang, Z. M.; Gao, S., An A-Site Mixed-Ammonium Solid Solution Perovskite Series of  $[(NH_2NH_3)_x(CH_3NH_3)_{1-x}][Mn(HCOO)_3]$  (x=1.00-0.67). Angew. Chem., Int. Ed. **2015**, *54*, 11093-11096.
- (26) Svane, K. L.; Forse, A. C.; Grey, C. P.; Kieslich, G.; Cheetham, A. K.; Walsh, A.; Butler, K. T. How Strong is the Hydrogen Bond in Hybrid Perovskites? *J. Phys. Chem. Lett.* **2017**, *8*, 6154-6159.
- (27) Šimėnas, M.; Ptak, M.; Khan, A. H.; Dagys, L.; Balevičius, V.; Bertmer, M.; Völkel, G.; Maczka, M.; Pöppl, A.; Banys, J. Spectroscopic Study of [(CH<sub>3</sub>)<sub>2</sub>NH<sub>2</sub>][Zn(HCOO)<sub>3</sub>] Hybrid Perovskite Containing Different Nitrogen Isotopes. *J. Phys. Chem. C* **2018**, *122*, 10284-10292.
- (28) Jaccard, C.; Kanzig, W.; Peter, M. Das Verhalten von Kolloidalen Seignetteelektrika .1. Kaliumphosphat KH<sub>2</sub>PO<sub>4</sub>. *Helv. Phys. Acta* **1953**, *26*, 521.
- (29) Lichtensteiger, C.; Dawber, M.; Triscone, J.-M. Ferroelectric size effects. In *Physics of Ferroelectrics: a Modern Perspective*; Springer: Berlin, 2007.
- (30) Ma, X.; Zhang, L.; Xu, G.; Zhang, C.; Song, H.; He, Y.; Zhang, C.; Jia, D. Facile Synthesis of NiS Hierarchical Hollow Cubes via Ni Formate Frameworks for High Performance Supercapacitors. *Chem. Eng. J.* **2017**, *320*, 22-28.
- (31) Ban, J. J.; Xu, G. C.; Zhang, L.; Lin, H.; Sun, Z. P.; Lv, Y.; Jia, D. Z. Mesoporous ZnO Microcube Derived from a Metal-Organic Framework as Photocatalyst for the Degradation of Organic Dyes. *J. Solid State Chem.* **2017**, *256*, 151-157.
- (32) Averback, C. M. Controlling phase behavior of coordination polymer networks and two-dimensional organic-inorganic compounds. Ph. D. Dissertation, University of Florida, Gainesville, FL, 2017
- (33) Rossin, A.; Ienco, A.; Costantino, F.; Montini, T.; Di Credico, B.; Caporali, M.; Gonsalvi, L.; Fornasiero, P.; Peruzzini, M. Phase Transitions and CO<sub>2</sub> Adsorption Properties of Polymeric Magnesium Formate. *Cryst. Growth Des.* **2008**, *8*, 3302-3308.
- (34) Stoilova, D.; Koleva, V. IR Study of Solid Phases Formed in the Mg(HCOO)<sub>2</sub>-Cu(HCOO)<sub>2</sub>-H<sub>2</sub>O System. *J. Mol. Struct.* **2000**, *553*, 131-139.
- (35) Abramoff, M. D.; Magalhaes, P. J.; Ram, S. J. Image Processing with ImageJ. *Biophotonics Int.* **2004**, *11*, 36.
- (36) Clausen, H. F.; Poulsen, R. D.; Bond, A. D.; Chevallier, M.-A. S.; Iversen, B. B. Solvothermal Synthesis of New Metal Organic Framework Structures in the Zinc-Terephthalic Acid-Dimethyl formamide System. *J. Solid State Chem.* **2005**, *178*, 3342-3351.
- (37) Wang, X.-Y.; Gan, L.; Zhang, S.-W.; Gao, S. Perovskite-Like Metal Formates with Weak Ferromagnetism and as Precursors to Amorphous Materials. *Inorg. Chem.* **2004**, *43*, 4615-4625.
- (38) Asaji, T.; Yoshitake, S.; Ito, Y.; Fujimori, H. Phase Transition and Cationic Motion in the Perovskite Formate Framework [(CH $_3$ ) $_2$ NH $_2$ ][Mg(HCOO) $_3$ ]. *J. Mol. Struct.* **2014**, *1076*, 719-723.

- (39) Dumont, M. F.; Knowles, E. S.; Guiet, A.; Pajerowski, D. M.; Gomez, A.; Kycia, S. W.; Meisel, M. W.; Talham, D. R. Photoinduced Magnetism in Core/Shell Prussian Blue Analogue Heterostructures of  $K_jNi_k[Cr(CN)_6]_rnH_2O$  with  $Rb_aCo_b[Fe(CN)_6]_c mH_2O$ . Inorg. Chem. **2011**, 50, 4295-4300.
- (40) Asakura, D.; Li, C. H.; Mizuno, Y.; Okubo, M.; Zhou, H. S.; Talham, D. R. Bimetallic Cyanide-Bridged Coordination Polymers as Lithium Ion Cathode Materials: Core@Shell Nanoparticles with Enhanced Cyclability. *J. Am. Chem. Soc.* **2013**, *135*, 2793-2799.
- (41) Ferreira, C. F.; Perez-Cordero, E. E.; Abboud, K. A.; Talham, D. R. Reversible Medium-Dependent Solid-Solid Phase Transformations in Two-Dimensional Hybrid Perovskites. *Chem. Mater.* **2016**, *28*, 5522-5529.
- (42) Frangville, C.; Gallois, M.; Li, Y.; Nguyen, H. H.; Viguerie, N. L. D.; Talham, D. R.; Mingotaud, C.; Marty, J.-D. Hyperbranched Polymer Mediated Size-Controlled Synthesis of Gadolinium Phosphate Nanoparticles: Colloidal Properties and Particle Size-Dependence on MRI Relaxivity. *Nanoscale* **2016**, *8*, 4252-4259.
- (43) Brinzari, T. V.; Rajan, D.; Ferreira, C. F.; Stoian, S. A.; Quintero, P. A.; Meisel, M. W.; Talham, D. R. Light-Induced Magnetization Changes in Aggregated and Isolated Cobalt Ferrite Nanoparticles. *J. Appl. Phys.* **2018**, *124*, 103904.
- (44) Felts, A. C.; Slimani, A.; Cain, J. M.; Andrus, M. J.; Ahir, A. R.; Abboud, K. A.; Meisel, M. W.; Boukheddaden, K.; Talham, D. R. Control of the Speed of a Light-Induced Spin Transition through Mesoscale Core-Shell Architecture. *J. Am. Chem. Soc.* **2018**, *140*, 5814-5824.
- (45) Rajan, D.; Cain, J. M.; Brinzari, T.; Ferreira, C. F.; Rudawski, N. G.; Felts, A. C.; Meisel, M. W.; Talham, D. R. Light-switchable exchange-coupled magnet. *ACS Appl. Electron. Mater.* **2019**, *1*, 2471-2475.
- (46) Panzer, F.; Bässler, H.; Lohwasser, R.; Thelakkat, M.; Köhler, A. The Impact of Polydispersity and Molecular Weight on the Order-Disorder Transition in Poly(3-hexylthiophene). *J. Phys. Chem. Lett.* **2014**, *5*, 2742-2747.
- (47) Šimėnas, M.; Balčiūnas, S.; Gonzalez-Nelson, A. Kinka, M.; Ptak, M.; van der Veen, M. A.; Mączka, M.; Banys, J. Preparation and Dielectric Characterization of P(VDF-TrFE) Copolymer-Based Composites Containing Metal-Formate Frameworks. *J. Phys. Chem. C* **2019**, *123*, 16380-16387.
- (48) Ma, Y.; Wang, Y.; Cong, J.; Sun, Y. Magnetic-Field Tuning of Hydrogen Bond Order-Disorder Transition in Metal-Organic Frameworks. *Phys. Rev. Lett.* **2019**, *122*, 255701.
- (49) Zhong, W. L.; Jiang, B.; Zhang, P. L.; Ma, J. M.; Cheng, H. M.; Yang, Z. H.; Li, L. X. Phase-Transitions in PbTiO<sub>3</sub> Ultrafine Particles of Different Sizes. *J. Phys.: Condens. Matter* **1993**, *5*, 2619-2624.
- (50) Zhong, W. L.; Wang, Y. G.; Zhang, P. L.; Qu, B. D. Phenomenological Study of the Size Effect on Phase-Transitions in Ferroelectric Particles. *Phys. Rev. B* **1994**, *50*, 698-703.
- (51) Asiaie, R.; Zhu, W.; Akbar, S. A.; Dutta, P. K. Characterization of Submicron Particles of Tetragonal BaTiO<sub>3</sub>. *Chem. Mater.* **1996**, *8*, 226-234.
- (52) Jiang, B.; Bursill, L. A. Phenomenological Theory of Size Effects in Ultrafine Ferroelectric Particles of Lead Titanate. *Phys. Rev. B* **1999**, *60*, 9978-9982.
- (53) Ma, W. Size Dependent Transition Enthalpy in PbTiO<sub>3</sub> Nanoparticles Due to a Cubic Surface Layer. *Appl. Phys. A: Mater. Sci. Process.* **2013**, *111*, 613-617.
- (54) Köferstein, R.; Walther, T.; Hesse, D.; Ebbinghaus, S. G. Crystallite-Growth, Phase Transition, Magnetic Properties, and Sintering Behaviour of Nano-CuFe<sub>2</sub>O<sub>4</sub> Powders Prepared by a Combustion-Like Process. *J. Solid State Chem.* **2014**, *213*, 57-64.

- (55) Zhang, W. J.; Xue, Y. Q.; Fu, Q. S.; Cui, Z. X.; Wang, S. T. Size Dependence of Phase Transition Thermodynamics of Nanoparticles: a Theoretical and Experimental Study. *Powder Technol.* **2017**, *308*, 258-265.
- (56) Cui, Z.; Duan, H.; Fu, Q.; Xue, Y.; Wang, S. Universal Size Dependence of Integral Enthalpy and Entropy for Solid-Solid Phase Transitions of Nanocrystals. *J. Phys. Chem. C* **2017**, *121*, 24831-24836.
- (57) Félix, G.; Nicolazzi, W.; Salmon, L.; Molnár, G.; Perrier, M.; Maurin, G.; Larionova, J.; Long, J.; Guari, Y.; Bousseksou, A. Enhanced Cooperative Interactions at the Nanoscale in Spin-Crossover Materials with a First-Order Phase Transition. *Phys. Rev.Lett.* **2013**, *110*, 235701.
- (58) Félix, G.; Mikolasek, M.; Molnár, G.; Nicolazzi, W.; Bousseksou, A. Control of the Phase Stability in Spin-Crossover Core-Shell Nanoparticles through the Elastic Interface Energy. *Eur. J. Inorg. Chem.* **2018**, 435-442.
- (59) Tolbert, S. H.; Alivisatos, A. P. Size Dependence of a First-Order Solid-Solid Phase-Transition the Wurtzite to Rock-Salt Transformation in CdSe Nanocrystals. *Science* **1994**, *265*, 373-376.
- (60) D'Avino, G.; Painelli, A.; Boukheddaden, K. Vibronic Model for Spin Crossover Complexes. *Phys. Rev. B* **2011**, *84*, 104119.
- (61) Chen, C.-C.; Herhold, A. B.; Johnson, C. S.; Alivisatos, A. P. Size Dependence of Structural Metastability in Semiconductor Nanocrystals. *Science* **1997**, *276*, 398-401.
- (62) Sánchez-Andújar, M.; Presedo, S.; Yánez-Vilar, S.; Castro-García, S.; Shamir, J.; Señarís-Rodríguez, M. A. Characterization of the Order-Disorder Dielectric Transition in the Hybrid Organic-Inorganic Perovskite-Like Formate Mn(HCOO)<sub>3</sub>[(CH<sub>3</sub>)<sub>2</sub>NH<sub>2</sub>]. *Inorg. Chem.* **2010**, *49*, 1510-1516.
- (63) Ptak, M.; Mączka, M.; Gągor, A.; Sieradzki, A.; Stroppa, A.; Di Sante, D.; Perez-Mato, J. M.; Macalik, L. Experimental and Theoretical Studies of Structural Phase Transition in a Novel Polar Perovskite-Like [C<sub>2</sub>H<sub>5</sub>NH<sub>3</sub>][Na<sub>0.5</sub>Fe<sub>0.5</sub>(HCOO)<sub>3</sub>] Formate. *Dalton Trans.* **2016**. *45*. 2574-2583.
- (64) Duncan, H. D.; Dove, M. T.; Keen, D. A.; Phillips, A. E. Local Structure of the Metal-Organic Perovskite Dimethylammonium Manganese(II) Formate. *Dalton Trans.* **2016**, *45*, 4380-4391.
- (65) Ptak, M.; Gagor, A.; Sieradzki, A.; Bondzior, B.; Dereń, P.; Ciupa, A.; Trzebiatowska, M.; Mączka, M. The Effect of K\* Cations on the Phase Transitions, and Structural, Dielectric and Luminescence Properties of [cat][K<sub>0.5</sub>Cr<sub>0.5</sub>(HCOO)<sub>3</sub>], Where Cat is Protonated Dimethylamine or Ethylamine. *Phys. Chem. Chem. Phys.* **2017**, *19*, 12156-12166.
- (66) Šimėnas, M.; Balčiūnas, S.; Trzebiatowska, M.; Ptak, M.; Mączka, M.; Völkel, G.; Pöppl, A.; Banys, J. Electron Paramagnetic Resonance and Electric Characterization of a [CH<sub>3</sub>NH<sub>2</sub>NH<sub>2</sub>][Zn(HCOO)<sub>3</sub>] Perovskite Metal Formate Framework. *J. Mater. Chem. C* **2017**, *5*, 4526-4536.
- (67) Collings, I.; Bykov, M.; Bykova, E.; Hanfland, M.; van Smaalen, S.; Dubrovinsky, L.; Dubrovinskaia, N. Disorder–order Transitions in the Perovskite Metal–organic Frameworks [(CH<sub>3</sub>)<sub>2</sub>NH<sub>2</sub>][M(HCOO)<sub>3</sub>] at High Pressure. *Cryst. Eng. Comm.* **2018**, *20*, 3512-3521.

### TOC Graphic

